Hindawi
Journal of Sensors
Volume 2019, Article ID 6074046, 8 pages
https://doi.org/10.1155/2019/6074046

Research Article

Facile Preparation of g-C_3N_4-WO_3 Composite Gas Sensing Materials with Enhanced Gas Sensing Selectivity to Acetone

Xiangfeng Chu,[1] **Junsong Liu**,[1] **Shiming Liang**,[2] **Linshan Bai**,[1] **Yongping Dong**,[1] **and Mauro Epifani**[3]

[1]*School of Chemistry and Chemical Engineering, Anhui University of Technology, Maanshan 243002, China*
[2]*School of Materials Science and Engineering, Linyi University, Linyi 276005, China*
[3]*Consiglio Nazionale delle Ricerche, Istituto per la Microelettronica ed i Microsistemi, Via Monteroni I-73100 Lecce, Italy*

Correspondence should be addressed to Xiangfeng Chu; xfchu99@ahut.edu.cn and Shiming Liang; lsmwind@163.com

Received 23 May 2019; Accepted 30 August 2019; Published 4 December 2019

Academic Editor: Bruno C. Janegitz

In this paper, g-C_3N_4-WO_3 composite materials were prepared by hydrothermal processing. The composites were characterized by means of X-ray powder diffraction (XRD), scanning electron microscopy (SEM), Fourier transform infrared spectroscopy (FTIR), X-ray photoelectron spectroscopy (XPS), and N_2 adsorption-desorption, respectively. The gas sensing properties of the composites were investigated. The results indicated that the addition of appropriate amount of g-C_3N_4 to WO_3 could improve the response and selectivity to acetone. The sensor based on 2 wt% g-C_3N_4-WO_3 composite showed the best gas sensing performances. When operating at optimum temperature of 310°C, the responses to 1000 ppm and 0.5 ppm acetone were 58.2 and 1.6, respectively, and the ratio of the $S_{1000\ ppm\ acetone}$ to $S_{1000\ ppm\ ethanol}$ reached 3.7.

1. Introduction

Graphitic carbon nitride (g-C_3N_4) nanomaterial exhibits a stable layered structure and π-conjugated s-triazine unit composed of sp^2 hybridized carbon atoms and sp^2 hybridized nitrogen atom. g-C_3N_4 nanosheets have attracted the attention of researchers in recent years for its peculiar properties as a semiconductor such as immense specific surface area [1]. Wang et al. [2] prepared g-C_3N_4 by thermal treatment of glucose and urea, and the p-type sensor based on g-C_3N_4 exhibited good response to NO_2 at room temperature.

As a gas sensing material, WO_3 has been paid much attention in the past decade. Cho et al. [3] used ultrasonic spray pyrolysis to prepare WO_3 hollow spheres using a citric acid-containing precursor solution; the WO_3 hollow spheres exhibited a high response and good gas sensing selectivity to trimethylamine, but the sensor exhibited a depressed response to NO_2. Kida et al. [4] used acidification of Na_2WO_4 with H_2SO_4 solution to prepare lamellar-structured WO_3 particles which had a high response ($S = 150–280$) even to dilute NO_2 (50–1000 ppb) in air at 200°C. A study by Ma et al. [5] showed that WO_3 nanoplates obtained through a topochemical transformation of the corresponding H_2WO_4 precursor exhibited high response to ethanol while operating at 300°C.

The photocatalytic activity of g-C_3N_4-WO_3 nanocomposites also has been reported by many researchers [6–9]; the photocatalytic performances of WO_3/g-C_3N_4 nanocomposites were higher than those of pure WO_3 and pure g-C_3N_4, which were attributed to the synergistic effect of WO_3 and pure g-C_3N_4. A study by Zhang et al. [10] showed that the ethanol sensing performance of α-Fe_2O_3/g-C_3N_4 nanocomposites was better than that of pure α-Fe_2O_3 and g-C_3N_4, which could be caused by porous α-Fe_2O_3 nanotubes wrapped by lamellar g-C_3N_4 nanostructures resulting in the formation of heterojunction. Cao et al. [11] reported that the gas sensing response and selectivity to ethanol could also be enhanced by modification of g-C_3N_4 nanosheets. The

combination of WO_3 and g-C_3N_4 may exhibit good gas sensing properties, which to the best of our knowledge has not been reported to date.

In this paper, we report the preparation of g-C_3N_4-WO_3 nanocomposites through a hydrothermal method and the investigation of their gas sensing properties. Analysis showed that 2 wt% g-C_3N_4-WO_3 nanocomposite responded highly and selectively to acetone.

2. Materials and Methods

2.1. Material Preparation and Characterization. g-C_3N_4 was prepared by heating 2.0 g melamine in an oven at 520°C for 5 hours, while keeping the heating rate at 5°C/min, which was similar to that reported in the literature [12]. After cooling to room temperature naturally, the product was purified with ethanol, following which it was dried at 60°C for 24 h succeeded by milling.

For preparing the nanocomposites, a certain amount of as-prepared g-C_3N_4 was added to 40 mL deionized water and sonicated for 1 hour to obtain a g-C_3N_4 suspension. 0.0025 mol $Na_2WO_4{\cdot}2H_2O$ was dissolved in 20 mL deionized water, and 4 mL concentrated hydrochloric acid was added dropwise in the Na_2WO_4 solution slowly while stirring resulting in the formation of H_2WO_4; the g-C_3N_4 suspension was added slowly to H_2WO_4 while stirring. The mixture was sealed in a 100 mL Teflon-lined stainless steel autoclave and heated at 200°C for 24 h; the obtained precipitate was filtered and washed with distilled water and ethanol, followed by drying in air at 80°C for 24 hours; finally, the g-C_3N_4-WO_3 composite was obtained. The weight ratios of g-C_3N_4 powders/WO_3 (the weight of WO_3 was calculated according to the weight of $Na_2WO_4{\cdot}2H_2O$) were 0 wt%, 1 wt%, 2 wt%, 3 wt%, and 4 wt% (the samples were labeled as S-0, S-1, S-2, S-3, and S-4, respectively).

X-ray diffraction (XRD, Bruker D8 Advance, Cu-Kα radiation: $\lambda = 0.15418$ nm), operating at 40 kV and 30 mA in a 2θ range from 10° to 70° at room temperature, was used to analyze the crystal structure of g-C_3N_4-WO_3 nanocomposites. A scanning electron microscope (SEM, Hitachi S-4800 microscope), with an accelerating voltage of 10 kV, was used to characterize the surface morphology of the samples. Fourier transform infrared spectroscopy (FTIR, Nicolet 6700 FTIR Spectrometer) spectra were recorded by the KBr pellet technique in the range 400–4000 cm^{-1}. The chemical species of elements were analyzed by X-ray photoelectron spectroscopy (XPS, Thermo ESCALAB250Xi) with all of the binding energies corrected according to contaminant carbon (C1s = 284.6 eV). The specific surface areas were characterized by the Brunauer-Emmett-Teller (BET, ASAP2010C) method using N_2 adsorption-desorption measurement.

2.2. Gas Sensing Measurement. The sensor device preparation process and the gas sensing measurement have been explained in the previous work [13]. The gas sensing response of the gas sensor was defined through the ratio of the resistance of the gas sensor in air (R_a) to that in the test gases (R_g). Figure S1, representing the gas sensor, is shown in supplementary materials.

3. Results and Discussion

3.1. Characterization. Figure 1 shows the XRD patterns of pure g-C_3N_4, g-C_3N_4-WO_3 (S-1, S-2, S-3, and S-4), and WO_3. Two significant diffraction peaks were observed at 13.23° and 27.86° in the XRD pattern of g-C_3N_4, indicating the (100) and (002) planes of layered g-C_3N_4; the weaker peak at 13.23° indicates the in-planar tris-s-triazine structural packing, and the stronger peak at 27.86° corresponds to the stacked of the aromatic systems between layers [6–8, 14]. All the diffraction peaks observed in XRD patterns of S-0, S-1, S-2, S-3, and S-4 could be indexed to the standard data of WO_3 (JCPDS 43-1035). The diffraction peaks of g-C_3N_4 could not be found because of the low concentration of g-C_3N_4 in the composites [14]. It was reported that the diffraction peaks of g-C_3N_4 did not appear in the XRD patterns of g-C_3N_4-WO_3 composites when the content of WO_3 was higher than 10 wt% [15]. The average crystallite sizes were calculated by the Scherrer formula:

$$D = \frac{K\lambda}{\beta \cos\theta}, \tag{1}$$

where D is the crystallite size, K is the instrument correction factor, γ is the Cu-Kα wavelength (0.151418 nm), β is the full width at half maximum of the peaks, and θ is the position of the peaks. The average crystallite sizes of WO_3 in S-0, S-1, S-2, S-3, and S-4 were 54.9, 62.6, 44.4, 44.3, and 50.2 nm, respectively. The calculated particle size of g-C_3N_4 was about 5.7 nm.

Figure 2 exhibits the SEM images of g-C_3N_4, pure WO_3 (S-0), and g-C_3N_4-WO_3 (S-2). The morphology of g-C_3N_4 was a sheet that consisted of small particles, and the particle sizes were about 200 nm. The WO_3 particle sizes in WO_3 and g-C_3N_4-WO_3 were between 100 and 400 nm; the addition of g-C_3N_4 in the composite had no obvious influence on the particle size of WO_3. The particle sizes obtained from SEM images were larger than those calculated from the Scherrer formula, which manifested that the particles observed by SEM in g-C_3N_4, pure WO_3, and g-C_3N_4-WO_3 were aggregates of smaller particles.

The FTIR spectra of WO_3 and g-C_3N_4-WO_3 (S-2) are shown in Figure 3. The absorption peaks at 763, 822, and 935 cm^{-1} in the spectra of two samples originated from stretching vibrations of O-W-O in WO_3 [9, 15, 16]; the peaks at 1632 and 3436 cm^{-1} in the FTIR spectra of WO_3 and g-C_3N_4-WO_3 (S-2) resulted from the vibration of bended H-O-H and stretched O-H of absorbed H_2O on the material surface [17]; and absorption peaks in the FTIR spectrum of g-C_3N_4-WO_3 (S-2), other than those of WO_3, at 1244, 1321, 1411, 1567, and 1632 cm^{-1} were ascribed to stretching vibration of C-NH-C and C=N of heterocycles [15], which proved the existence of g-C_3N_4 in the composite. The XPS results were discussed in the supplementary materials, which could prove the formation of g-C_3N_4-WO_3.

3.2. Gas Sensing Characterization. The gas sensing responses of pure WO_3, S-1, S-2, S-3, and S-4 to 1000 ppm concentration of acetone at different operating temperatures are shown

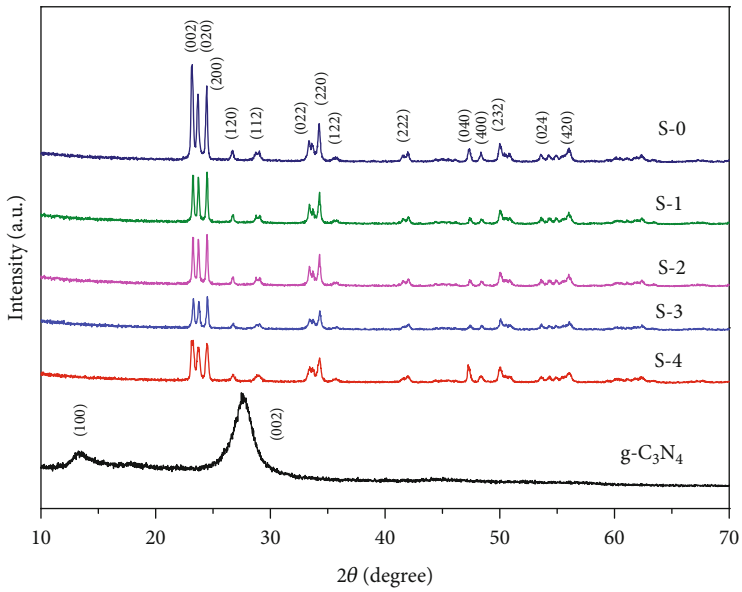

Figure 1: The XRD patterns of pure g-C_3N_4, g-C_3N_4-WO_3 (S-1, S-2, S-3, and S-4), and WO_3.

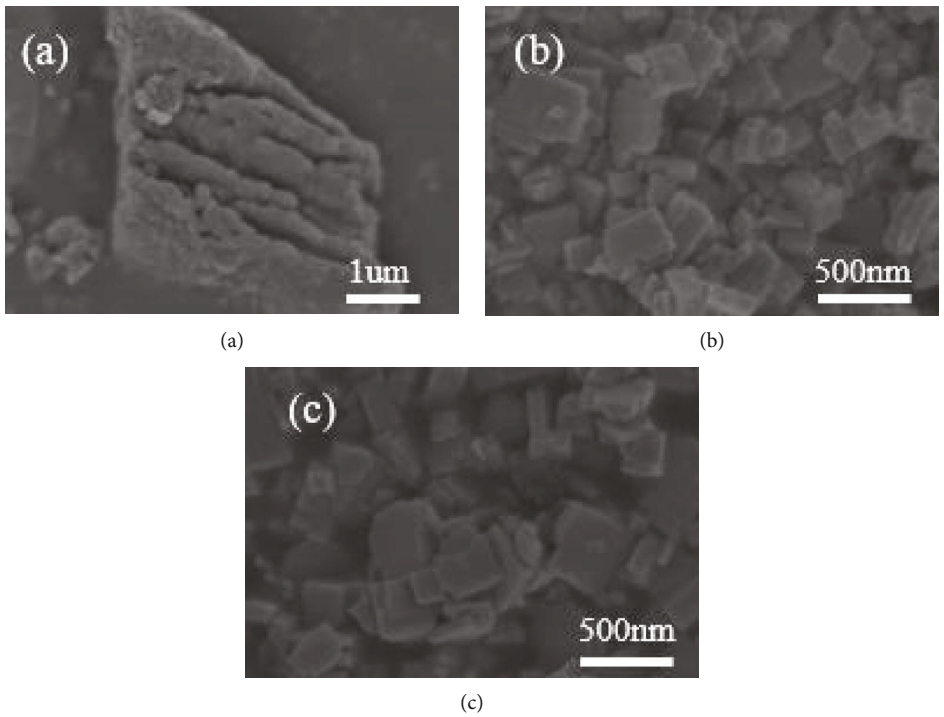

(a) (b)

(c)

Figure 2: The SEM images of (a) g-C_3N_4, (b) pure WO_3 (S-0), and (c) g-C_3N_4-WO_3 (S-2).

in Figure 4. An increase in the response with an increase in the amount of g-C_3N_4 in the g-C_3N_4-WO_3 composite was observed while the content of g-C_3N_4 was lower than 2 wt%; when the contents of g-C_3N_4 in the g-C_3N_4-WO_3 composite were 3 wt% and 4 wt%, the responses decreased significantly; the optimal operating temperatures for S-1 and S-2 were all 310°C, which were better than that for pure WO_3. The responses of pure WO_3, S-1, S-2, S-3, and S-4 to 1000 ppm acetone at 310°C were 3.7, 16.2, 58.2, 1.0, and 1.3, respectively. It has been reported that pure g-C_3N_4 exhibited very little response to acetone; the response improved significantly for a particular content of g-C_3N_4 in a series of g-C_3N_4-SnO_2 nanocomposites [18]. The response of α-Fe_2O_3/g-C_3N_4 to ethanol was also reported [11]; an appropriate amount of g-C_3N_4 in the composites was propitious to the dispersion of α-Fe_2O_3 in the composites and the formation of better heterojunctions; the reasons for the enhancement of gas sensing response were attributed to the larger specific surface area, better permeability, and heterojunction. A sensor based on the S-2 composite

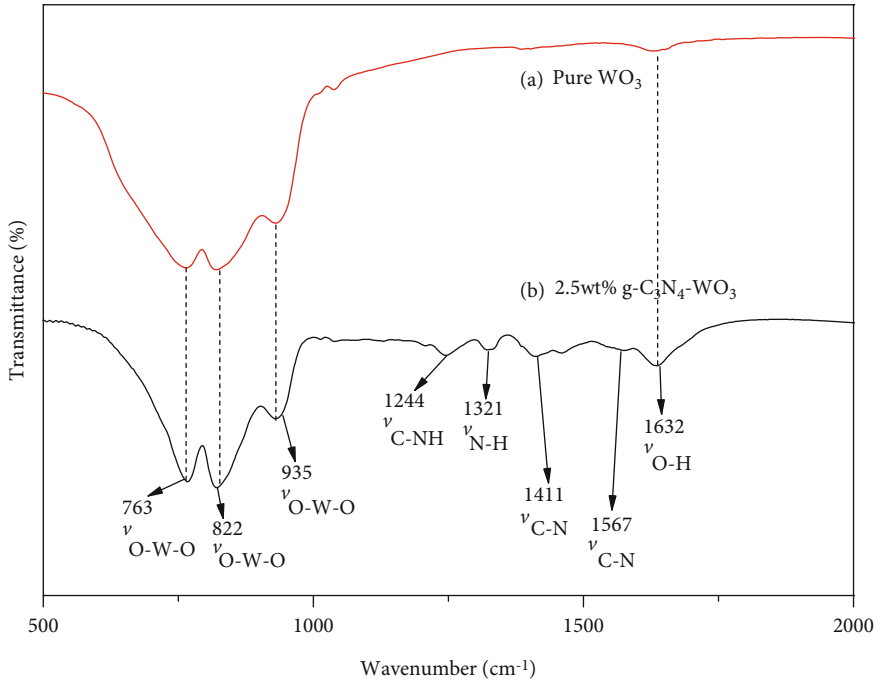

Figure 3: The FTIR spectra of WO_3 and g-C_3N_4-WO_3 (S-2).

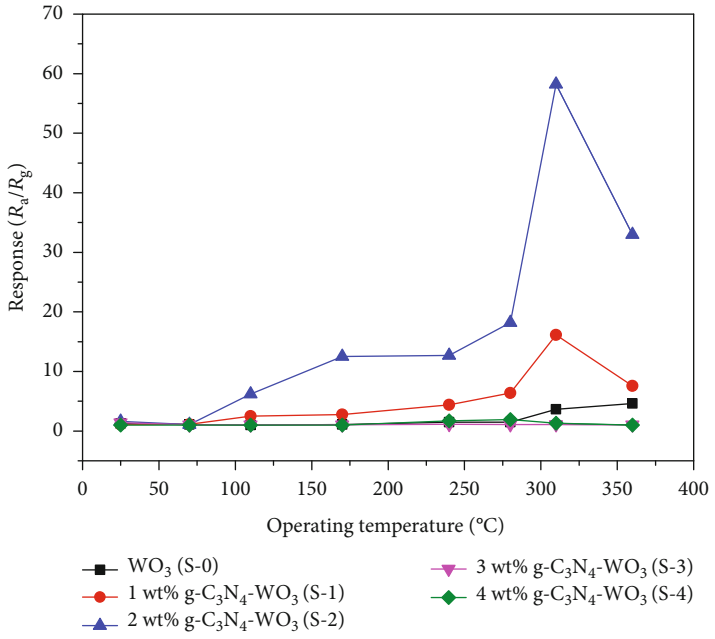

Figure 4: The gas sensing responses of pure WO_3, S-1, S-2, S-3, and S-4 to 1000 ppm acetone at different temperatures.

exhibited higher response to acetone compared with pure WO_3. The N_2 adsorption-desorption results are shown in Figure S3 of supplementary materials; the average pore size difference between S-0 and S-2 was not obvious, and the gas diffusion rates in the inner sections of S-0 and S-2 were approximate; the enhancement of gas sensing response of S-2 was probably attributable to the larger specific surface area of S-2 and heterojunction. Many literatures have reported the acetone sensing mechanism of WO_3 [19, 20], and the conductance of the WO_3 sensor is influenced by the changes in chemisorbed oxygen present on the surface of the gas sensing material; on exposure of a sensor to air, oxygen is adsorbed on the surface of WO_3, which in turn captured electrons from the conduction band of WO_3, resulting in the decrease in electron concentration in the conduction band; oxygen molecules changes into $O_2^-{}_{(ads)}$, $O^-{}_{(ads)}$, and $O^{2-}{}_{(ads)}$ with variation of temperature. When the sensor was placed in an acetone

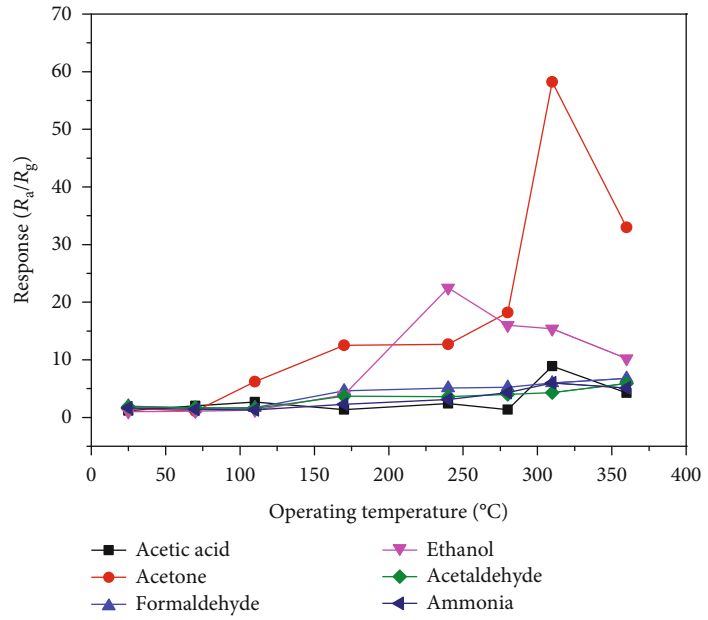

Figure 5: The responses of an S-2-based sensor to 1000 ppm acetic acid, acetone, formaldehyde, ethanol, acetaldehyde, and ammonia at different operating temperatures.

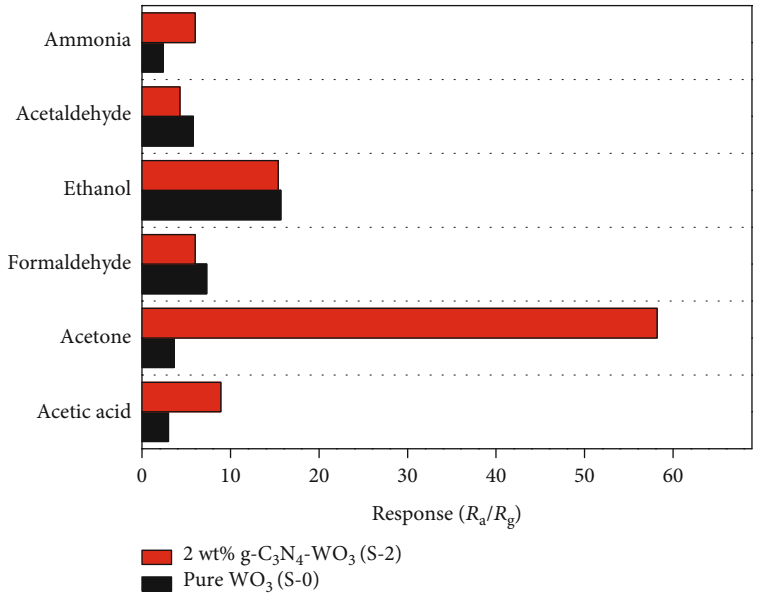

Figure 6: The responses of sensors based on S-0 and S-2 to six kinds of gases (1000 ppm) at 310°C.

vapor atmosphere, acetone reacted with $O_2^-{}_{(ads)}$, $O^-{}_{(ads)}$, and $O^{2-}{}_{(ads)}$, releasing the electrons captured by oxygen molecules to the conduction band of WO_3 and decreasing the resistance of the sensor. The reaction is as follows:

$$CH_3COCH_3 + 4\,O_2^-(\text{ads}) = 3CO_2 + 3H_2O + 4\,e \quad (2)$$

Figure 5 depicts the responses of an S-2-based sensor to 1000 ppm acetic acid, acetone, formaldehyde, ethanol, acetaldehyde, and ammonia at different temperatures. The optimal operating temperatures for formaldehyde, ethanol, and acetaldehyde were 360°C, 240°C, and 360°C, respectively; the maximum responses for acetic acid, acetone, and ammonia all appeared at 310°C. At an operating temperature of 310°C, the responses to 1000 ppm acetic acid, acetone, formaldehyde, ethanol, acetaldehyde, and ammonia were 8.9, 58.2, 6.0, 15.4, 4.3, and 6.0, respectively; the S-2 sensor showed significant gas sensing selectivity to acetone, with the response ratio of $S_{1000\ \text{ppm acetone}}/S_{1000\ \text{ppm ethanol}}$ reaching 3.8.

Figure 6 shows the responses of S-0- and S-2-based sensors to six kinds of gases, while keeping the concentration

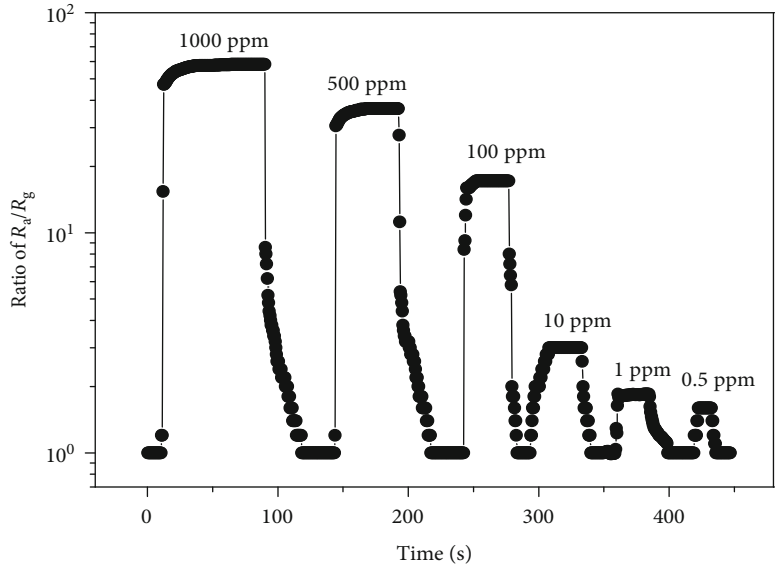

Figure 7: The response transients of the sensor based on the sample S-2 composite to acetone (1000 ppm, 500 ppm, 100 ppm, 10 ppm, 1 ppm, and 0.5 ppm) at 310°C.

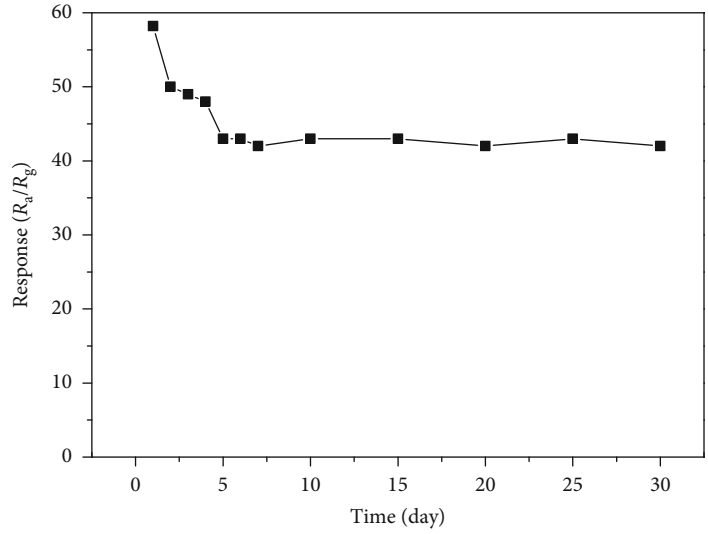

Figure 8: The curve of gas sensing response versus time of the S-2 sensor.

1000 ppm, at 310°C. The responses of the S-2 sensor to acetaldehyde, ethanol, and formaldehyde were lower than those of the pure WO_3 sensor. But the responses of the S-2 sensor to ammonia, acetone, and acetic acid were higher than those of the pure WO_3 gas sensor; especially, the response of the S-2 sensor to acetone was 15 times that of the pure WO_3 gas sensor, proving the role of g-C_3N_4 in improving the selectivity of the gas sensor.

The response time and recovery time were calculated using the formula defined in a previous literature [21]. The response curve transients of the sensor based on the sample S-2 composite to acetone (1000 ppm, 500 ppm, 100 ppm, 10 ppm, 1 ppm, and 0.5 ppm) at 310°C are shown in Figure 7. The responses to 1000 ppm, 500 ppm, 100 ppm, 10 ppm, 1 ppm, and 0.5 ppm acetone were 58.2, 36.6, 17.2, 3.0, 1.8, and 1.6, respectively; the detection limit of the S-2 composite-based sensor to acetone was 0.5 ppm. The response times for 1000, 500, 100, 10, 1, and 0.5 ppm acetone were 53, 24, 10, 15, 7, and 5 s, respectively, while the recovery times for 1000, 500, 100, 10, 1, and 0.5 ppm acetone were 29, 25, 6, 7, 12, and 3 s, respectively. The acetone concentration in the breath varies from 0.3 to 0.9 ppm for healthy people, but the acetone concentration exceeds 1.8 ppm for diabetic patients [22]. The S-2 composite-based sensor had a response of 1.6 to 0.5 ppm acetone which meant that it has the potential for application in diabetes detection.

The gas sensor stability is a significant parameter for a gas sensor, and the curve of gas sensing response versus time of the S-2 composite-based sensor is shown in Figure 8. The gas sensing response decreased significantly in seven days and then achieved stability between the seventh and thirtieth days. The stability of the sensor can be improved further. The

Table 1: Comparison of acetone gas sensing properties with different acetone gas sensors.

Material	Operating temperature (°C)	Detection limit (ppm)	Response (R_a/R_g) (concentration)	Selectivity	Stability (days)	Reference
Au/ZnO	365	20	2923 (100 ppm)	1.8	90	[23]
$MgFe_{2-x}Ce_xO_4$	700	100	1.91 (2000 ppm)	1.2	-	[24]
Co_3O_4 NWS-HCSs	150	1	23 (200 ppm)	4.6	-	[25]
$PrFeO_3$	180	10	141 (200 ppm)	2.8	75	[26]
Pt-Fe_2O_3	139	0.2	25.7 (100 ppm)	2.9	15	[27]
Rh- doped SnO_2	200	1	60.6 (50 ppm)	8.6	-	[28]
$ZnFe_2O_4$	260	10	52.8 (100 ppm)	3.2	30	[29]
g-C_3N_4-WO_3	310	0.5	58.2 (1000 ppm)	3.7	30	This work

"-" means no data available in the literature.

g-C_3N_4-WO_3 composite (S-2) has proven itself to be a potential candidate for application as an acetone sensor, if the stability of the sensor can be improved.

Table 1 compares the gas sensing properties of different acetone sensors. Overall, the g-C_3N_4-WO_3 acetone gas sensor showed good sensitivity to acetone and also had significant selectivity. Besides, the detection limit is as low as 0.5 ppm which is the second lowest in the listed acetone sensor.

4. Conclusions

It can be observed that the content of g-C_3N_4 in g-C_3N_4-WO_3 composites influences the response and selectivity of g-C_3N_4-WO_3 composite-based sensors to acetone. 2 wt% g-C_3N_4-WO_3 composite (S-2) showed the best gas sensing performances in the series of g-C_3N_4-WO_3 composites, when operating at an optimum temperature of 310°C; the responses to 1000 ppm and 0.5 ppm acetone were 58.2 and 1.6, respectively, with the ratio of the $S_{1000\ ppm\ acetone}$ to $S_{1000\ ppm\ ethanol}$ reaching 3.7; the S-2 composite-based sensor was able to detect acetone at concentrations as low as 0.5 ppm. The sensor took 5 s and 3 s to respond to 0.5 ppm acetone and to recover; the g-C_3N_4-WO_3 composite (S-2) has proven to be a potential candidate for application as an acetone sensor if the stability of the sensor can be improved.

Data Availability

The underlying data related to this manuscript is available on request.

Conflicts of Interest

The authors declare no conflict of interest.

Acknowledgments

This research was funded by the National Natural Science Foundation of China (Nos. 61671019 and 61971003).

Supplementary Materials

Figure S1: gas sensor used for characterizing gas sensing behavior of samples. Figure S2: XPS spectra of g-C_3N_4-WO_3 (S-2): (a) full spectrum. (b) C1s. (c) N1s. (d) O1s. (e) W. Figure S3: (a) N_2 adsorption-desorption isotherm of WO_3. (b) Pore size distribution curve of WO_3. (c) N_2 adsorption-desorption isotherm of g-C_3N_4-WO_3 (S-2). (d) Pore size distribution curve of g-C_3N_4-WO_3 (S-2). *(Supplementary Materials)*

References

[1] L. Yang, X. Liu, Z. Liu et al., "Enhanced photocatalytic activity of g-C_3N_4 2D nanosheets through thermal exfoliation using dicyandiamide as precursor," *Ceramics International*, vol. 44, no. 17, pp. 20613–20619, 2018.

[2] D. Wang, W. Gu, Y. Zhang et al., "Novel C-rich carbon nitride for room temperature NO_2 gas sensors," *RSC Advances*, vol. 4, no. 35, pp. 18003–18006, 2014.

[3] Y. H. Cho, Y. C. Kang, and J. H. Lee, "Highly selective and sensitive detection of trimethylamine using WO_3 hollow spheres prepared by ultrasonic spray pyrolysis," *Sensors and Actuators B: Chemical*, vol. 176, pp. 971–977, 2013.

[4] T. Kida, A. Nishiyama, M. Yuasa, K. Shimanoe, and N. Yamazoe, "Highly sensitive NO_2 sensors using lamellar-structured WO_3 particles prepared by an acidification method," *Sensors and Actuators B: Chemical*, vol. 135, no. 2, pp. 568–574, 2009.

[5] J. Ma, J. Zhang, S. Wang et al., "Topochemical preparation of WO_3 nanoplates through precursor H_2WO_4 and their gas-sensing performances," *The Journal of Physical Chemistry C*, vol. 115, no. 37, pp. 18157–18163, 2011.

[6] K. Katsumata, R. Motoyoshi, N. Matsushita, and K. Okada, "Preparation of graphitic carbon nitride (g-C_3N_4)/WO_3 composites and enhanced visible-light-driven photodegradation of acetaldehyde gas," *Journal Hazardous Materials*, vol. 260, pp. 475–482, 2013.

[7] Z. Jin, N. Murakami, T. Tsubota, and T. Ohno, "Complete oxidation of acetaldehyde over a composite photocatalyst of graphitic carbon nitride and tungsten(VI) oxide under visible-light irradiation," *Applied Catalysis B: Environmental*, vol. 150-151, pp. 479–485, 2014.

[8] H. Katsumata, Y. Tachi, T. Suzuki, and S. Kaneco, "Z-scheme photocatalytic hydrogen production over WO_3/g-C_3N_4 composite photocatalysts," *RSC Advances*, vol. 4, no. 41, pp. 21405–21409, 2014.

[9] M. Karimi-Nazarabad and E. K. Goharshadi, "Highly efficient photocatalytic and photoelectrocatalytic activity of solar light driven WO_3/g-C_3N_4 nanocomposite," *Solar Energy Materials & Solar Cells*, vol. 160, pp. 484–493, 2017.

[10] Y. Zhang, D. Zhang, W. Guo, and S. Chen, "The α-Fe_2O_3/g-C_3N_4 heterostructural nanocomposites with enhanced ethanol gas sensing performance," *Journal of Alloys and Compounds*, vol. 685, pp. 84–90, 2016.

[11] J. Cao, C. Qin, Y. Wang et al., "Synthesis of g-C_3N_4 nanosheet modified SnO_2 composites with improved performance for ethanol gas sensing," *RSC Advances*, vol. 7, no. 41, pp. 25504–25511, 2017.

[12] X. Wang, K. Maeda, A. Thomas et al., "A metal-free polymeric photocatalyst for hydrogen production from water under visible light," *Nature Materials*, vol. 8, no. 1, pp. 76–80, 2009.

[13] X. Chu, J. Wang, L. Bai, Y. Dong, W. Sun, and W. Zhang, "Trimethylamine and ethanol sensing properties of $NiGa_2O_4$ nano-materials prepared by co-precipitation method," *Sensors and Actuators B: Chemical*, vol. 255, pp. 2058–2065, 2018.

[14] F. Zhan, R. Xie, W. Li et al., "*In situ* synthesis of g-C_3N_4/WO_3 heterojunction plates array films with enhanced photoelectrochemical performance," *RSC Advances*, vol. 5, no. 85, pp. 69753–69760, 2015.

[15] J. Ding, Q. Liu, Z. Zhang et al., "Carbon nitride nanosheets decorated with WO_3 nanorods: ultrasonic-assisted facile synthesis and catalytic application in the green manufacture of dialdehydes," *Applied Catalysis B: Environmental*, vol. 165, pp. 511–518, 2015.

[16] H. Xu, L. Liu, X. She et al., "WO_3 nanorod photocatalysts decorated with few-layer g-C_3N_4 nanosheets: controllable synthesis and photocatalytic mechanism research," *RSC Advances*, vol. 6, no. 83, pp. 80193–80200, 2016.

[17] S. P. Adhikari, H. R. Pant, H. J. Kim, C. H. Park, and C. S. Kim, "Deposition of ZnO flowers on the surface of g-C_3N_4 sheets via hydrothermal process," *Ceramics International*, vol. 41, no. 10, pp. 12923–12929, 2015.

[18] J. Hu, C. Zou, Y. Su et al., "One-step synthesis of 2D C_3N_4-tin oxide gas sensors for enhanced acetone vapor detection," *Sensors and Actuators B: Chemical*, vol. 253, pp. 641–651, 2017.

[19] D. Chen, X. Hou, T. Li et al., "Effects of morphologies on acetone-sensing properties of tungsten trioxide nanocrystals," *Sensors and Actuators B: Chemical*, vol. 153, no. 2, pp. 373–381, 2017.

[20] J. Kaur, K. Anand, A. Kaur, and R. C. Singh, "Sensitive and selective acetone sensor based on Gd doped WO_3/reduced graphene oxide nanocomposite," *Sensors and Actuators B: Chemical*, vol. 258, pp. 1022–1035, 2018.

[21] X. Chu, P. Dai, S. Liang, A. Bhattacharya, Y. Dong, and M. Epifani, "The acetone sensing properties of ZnFe2O4-graphene quantum dots (GQDs) nanocomposites at room temperature," *Physica E: Low-dimensional Systems and Nanostructures*, vol. 106, pp. 326–333, 2019.

[22] S. K. Rai, K. W. Kao, S. Gwo, A. Agarwal, W. D. Lin, and J. A. Yeh, "Indium nitrite (InN)-based ultrasensitive and selective ammonia sensor using an external silicone oil filter for medical application," *Sensors*, vol. 18, no. 11, p. 3887, 2018.

[23] P. Wang, T. Dong, C. Jia, and P. Yang, "Ultraselective acetone-gas sensor based ZnO flowers functionalized by Au nanoparticle loading on certain facet," *Sensors and Actuators B: Chemical*, vol. 288, pp. 1–11, 2019.

[24] J. Y. Patil, D. Y. Nadargi, I. S. Mulla, and S. S. Suryavanshi, "Cerium doped $MgFe_2O_4$ nanocomposites: highly sensitive and fast response-recoverable acetone gas sensor," *Heliyon*, vol. 5, no. 6, article e01489, 2019.

[25] C. Zhang, L. Li, L. Hou, and W. Chen, "Fabrication of Co_3O_4 nanowires assembled on the surface of hollow carbon spheres for acetone gas sensing," *Sensors and Actuators B: Chemical*, vol. 291, pp. 130–140, 2019.

[26] L. Ma, S. Y. Ma, X. F. Shen et al., "$PrFeO_3$ hollow nanofibers as a highly efficient gas sensor for acetone detection," *Sensors and Actuators B: Chemical*, vol. 255, pp. 2546–2554, 2018.

[27] S. Zhang, M. Yang, K. Liang et al., "An acetone gas sensor based on nanosized Pt-loaded Fe_2O_3 nanocubes," *Sensors and Actuators B: Chemical*, vol. 290, pp. 59–67, 2019.

[28] X. Kou, N. Xie, F. Chen et al., "Superior acetone gas sensor based on electrospun SnO_2 nanofibers by Rh doping," *Sensors and Actuators B: Chemical*, vol. 256, pp. 861–869, 2018.

[29] L. Li, J. Tan, M. Dun, and X. Huang, "Porous $ZnFe_2O_4$ nanorods with net-worked nanostructure for highly sensor response and fast response acetone gas sensor," *Sensors and Actuators B: Chemical*, vol. 248, pp. 85–91, 2017.